nature electronics

ARTICLES

https://doi.org/10.1038/s41928-019-0304-4

Three-dimensional curvy electronics created using conformal additive stamp printing

Kyoseung Sim[1], Song Chen[1], Zhengwei Li[2], Zhoulyu Rao[3], Jingshen Liu[4], Yuntao Lu[3], Seonmin Jang[3], Faheem Ershad[5], Ji Chen[4], Jianliang Xiao[2] and Cunjiang Yu[1,3,4,5,6*]

Electronic devices are typically manufactured in planar layouts, but many emerging applications, from optoelectronics to wearables, require three-dimensional curvy structures. However, the fabrication of such structures has proved challenging due, in particular, to the lack of an effective manufacturing technology. Here, we show that conformal additive stamp (CAS) printing technology can be used to reliably manufacture three-dimensional curvy electronics. CAS printing employs a pneumatically inflated elastomeric balloon as a conformal stamping medium to pick up pre-fabricated electronic devices and print them onto curvy surfaces. To illustrate the capabilities of the approach, we use it to create various devices with curvy shapes: silicon pellets, photodetector arrays, electrically small antennas, hemispherical solar cells and smart contact lenses. We also show that CAS printing can be used to print onto arbitrary three-dimensional surfaces.

The dominant form of electronics—microelectronics—traditionally creates devices with planar layouts. There are, however, many devices that require three-dimensional (3D) shapes and whose performances and functionalities are strongly coupled with their geometrical form factors. Examples include imagers with curved focal planes[1–4], smart contact lenses with curvilinear shapes[5–7] and antennas with non-planar designs[8–10]. These devices, which can have size on the scale of millimetres to centimetres and features on the order of micrometres, are challenging to build. The major hurdle lies in the lack of a versatile manufacturing technology that can reliably construct 3D curvy electronics.

Existing manufacturing technologies, such as microfabrication, cannot achieve 3D curvilinear electronics due to the inherently 2D nature of their wafer-based planar processes. Some emerging manufacturing technologies could potentially address the challenge directly or indirectly, but they all suffer from deficiencies. For example, deterministic folding processes can deform a predefined 2D sheet into 3D shapes[11–14], but the approach has limited access to non-developable shapes, such as spherical or arbitrary complex curvilinear shapes. Three-dimensional printing has been exploited to manufacture electronics by delivering electronic inks directly onto curved surfaces[8,15–17]. However, 3D printing is mainly applicable for slurry-based inks of conductors and semiconductors, and the fabricated devices cannot offer performance comparable to a device fabricated with wafer-based technologies, due to the inherent material limitations such as lower conductivity of the conductors and low carrier mobility of the semiconductors[18–21]. Another approach involves pre-stretching and flattening a curvy elastomeric membrane as a temporary flat substrate for planar device fabrication and then releasing it to form curved shapes[22–24]. However, rubber is one of the few materials that can be stretched from curvy to flat shapes, even if the large mechanical strain associated with the flattening and restoring steps is disregarded. Therefore, the approach restricts its general usage and visibility. Pad printing, a technology primarily used for graphic printing, allows the direct printing of wet or slurry inks onto curvy surfaces, which has recently been extended into 3D antenna fabrication[25]. However, the associated ink materials and pad mechanics limit its use in high-performance curvy electronics.

Here, we report a manufacturing technology, called conformal additive stamp (CAS) printing and show that it can be used to reliably manufacture devices with 3D shapes. Our CAS printing approach employs a pneumatically inflated elastomeric balloon as a conformal stamping medium to pick up the pre-fabricated electronic devices (that is, inks) in 2D geometries from microfabrication and then deliver them onto arbitrary curvilinear 3D surfaces. The process (Fig. 1a) involves first approaching a pneumatically inflated balloon stamp to the fabricated inks. The stamp is then brought into intimate contact with the fabricated inks. Due to the excellent deformability, the balloon stamp is able to conformably contact and pick up the inks when peeled off. The inked balloon stamp is then brought into contact with the target 3D curvilinear surfaces to directly deliver or print the inks on. The deformability of the elastomeric balloon allows it to form intimate contact with complex 3D surfaces and thus, it can print inks on 3D substrates.

There are some similarities in operation procedures between CAS printing and pad printing (a detailed comparison is provided in Supplementary Note 1 and Supplementary Table 1). However, the distinct features of CAS printing are that it allows high-performance electronics to be constructed by taking the advantage of microfabrication and it can be used to manufacture on random 3D curvy shapes. To highlight the key aspects, fidelity and versatility of CAS printing, we provide a systematic experimental, computational and analytical examination of the technology and demonstrate that it can be used to fabricate devices ranging from isolated pixel arrays to interconnected functional systems.

CAS printing of Si pellet array

Figure 1a shows a schematic of CAS printing of a Si pellet array. The process involves preparing a Si pellet array on a temporary substrate, picking up the array using a balloon stamp and printing

[1]Department of Mechanical Engineering, University of Houston, Houston, TX, USA. [2]Department of Mechanical Engineering, University of Colorado, Boulder, CO, USA. [3]Materials Science and Engineering Program, University of Houston, Houston, TX, USA. [4]Department of Electrical and Computer Engineering, University of Houston, Houston, TX, USA. [5]Department of Biomedical Engineering, University of Houston, Houston, TX, USA. [6]Texas Center for Superconductivity, University of Houston, Houston, TX, USA. *e-mail: cyu15@uh.edu

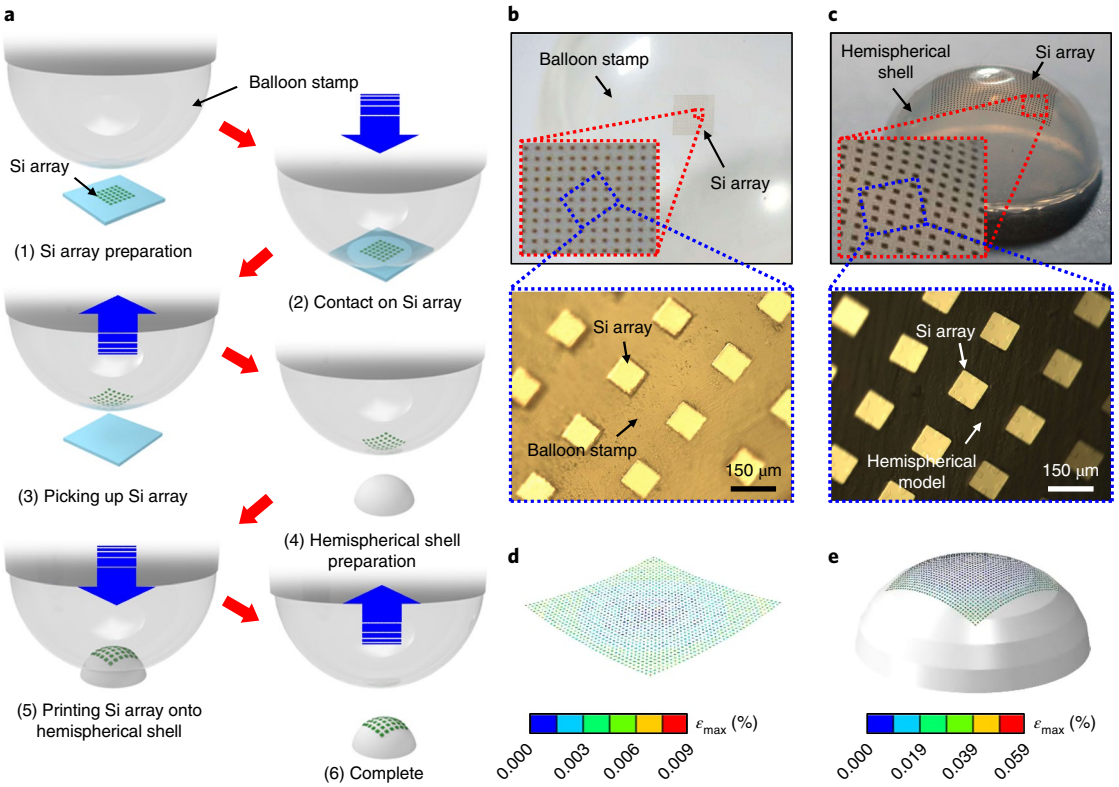

Fig. 1 | CAS printing. a, Schematic of CAS printing. **b**, The optical (top) and optical microscope (bottom) images of the retrieved Si pellet array on a balloon stamp. Inset: magnified view of Si pellet array. **c**, The optical (top) and optical miscroscope (bottom) images of CAS-printed Si pellet array on a hemispherical shell. Inset: magnified view of Si pellet array. **d**, Maximum principal strain (ε_{max}) contour in the Si pellet array on a balloon stamp after picking up from an SOI wafer. **e**, Maximum principal strain contour in the Si pellet array on a hemispherical Ecoflex shell after CAS printing.

the array onto a 3D curvy surface. The Si pellet array (39 × 39, each pellet size 100 μm × 100 μm) was fabricated based on a silicon-on-insulator (SOI) wafer with 1.25-μm-thick top Si layer. The processes mainly include photolithography and reactive-ion etching (RIE) to define the pellet geometries, formation of photoresist anchors as temporary tethers and undercut etching of the buried oxide in concentrated hydrofluoric acid (49%) to separate the pellets from the substrate. The detailed processes are described in the Methods and Supplementary Fig. 1. A photograph and optical microscope image of the prepared Si pellet array on a wafer are shown in Supplementary Fig. 2. The balloon stamp was prepared by coating a thin layer (~271 μm) of Clearflex (Smooth-On, Clear Flex 50) on the surface of a commercially available latex balloon (Qualatex, 5″ round). Clearflex was chosen because of two major reasons: (1) the ability to coat on the latex balloon surface and (2) modifiable surface adhesion for picking up and printing.

A custom-made CAS printing platform is shown in Supplementary Fig. 3. The balloon stamp is able to move up and down. The prepared balloon stamp was moved down to press against the wafer to contact with the array and then the stamp was lifted off to pick up the array from the wafer. The temporary photoresist tethers were broken due to the adhesion between the pellet and Clearflex[26–28]. Figure 1b shows the images of the Si pellet array on the balloon stamp after picking up. The Si pellet array was finally printed onto a hemispherical Ecoflex (Smooth-On Ecoflex 00-30) shell, which was prepared based on a moudling process (Supplementary Fig. 4). It is noted that the outer surface of the hemispherical shell was treated by ultraviolet ozone for 10 min to generate hydroxyl terminal groups, which allow for covalent bonding with Si pellets. Similar surface treatment was employed in other studies[29–31]. Figure 1c shows the image of the Si pellet array on the hemispherical shell. The inset is the optical microscope image. It is noted that no cracks or damage of the Si pellets was observed during the CAS printing process, based on the scanning electron microscope (XL-30S FEG, Philips) image as shown in Supplementary Fig. 5. In addition, the CAS printing shows high yield (>99%). Supplementary Fig. 6 shows a representative image of the Si array printed on a hemispherical shell.

The associated deformation and strain in both the balloon stamp and the Si pellet array during and after CAS printing were investigated by finite-element analysis (FEA). The details of the FEA are described in Supplementary Note 2. Supplementary Fig. 7 shows the displacement contour of the Si pellet array on the balloon stamp after picking up. The relative displacements of Si pellets caused by picking up are very small due to the much smaller size of the Si pellet array compared with that of the balloon stamp, resulting in minimal array distortion at the periphery of the array (Supplementary Fig. 8). The maximum principal strain (ε_{max}) contour of the Si pellet array on the balloon stamp after picking up is shown in Fig. 1d and Supplementary Fig. 9a (top view). The strain in all the Si pellets is less than 0.01%, which is far smaller than the fracture strain of Si (~1%)[32,33]. The strain contours of the balloon and Clearflex outer layer after picking up the Si pellet array are shown in Supplementary Fig. 9b,c, respectively. The magnitude of the relative displacement contour of the Si pellet array after CAS printing on the hemispherical Ecoflex shell is shown in Supplementary Fig. 10a. The corresponding strain distribution is shown in Fig. 1e and Supplementary Figs. 10b (top view) and 11 (perspective view).

The results show that the central region of the array has relatively lower strain than the peripheral area because the deformation in the balloon stamp increases from the initial contact region (central region of the array) to the outer areas. During conformal contact of

the stamp, the central region of the array contacts on the top/centre of the hemispherical shell and thus the deformation is restrained, while the periphery region of the array further deforms with the balloon stamp before contacting to the shell. The deformation and strain distribution in the latex balloon and Clearflex layer during transfer printing are shown in Supplementary Fig. 12. The Si pellet array originally in a planar configuration conforms to the curvy balloon stamp (after picking up) and the targeted hemispherical shell (after printing) surfaces; therefore, position distortion happens mainly in the peripheral area. Supplementary Fig. 13 compares the top views of the array prepared on the Si wafer (grey) and after CAS printing onto the curvy shell (green). Direct comparisons between experiment and simulations suggest that the distortions are very small, as shown in Supplementary Fig. 14. These distortions can be potentially eliminated and corrected through the following means: (1) improving the accuracy of the balloon stamp and hemispherical receiver substrate to allow better match between the experiment and simulation; (2) equipping the CAS printing with a high-accuracy camera and translation stage to allow accurate alignment.

To further investigate the areal coverage level of the printed Si pellet array, we performed FEA simulations with a representative unit of 3 × 3 Si pellet array atop the elastomeric balloon stamp under 11% equal biaxial tension (Supplementary Fig. 12c). Supplementary Fig. 15a shows the strain contours with varying spacing of 250, 100 and 10 μm, respectively. With the decrease of spacing, the maximum strain increases slightly but is still far below the fracture strain of ~1% of Si (Supplementary Fig. 15b). The relationship between the maximum strain and areal coverage in the Si pellet is given in Supplementary Fig. 15c, which shows that the areal coverage can reach as high as 82.6% (that is, the spacing is 10 μm) with an insignificant, low strain level (Supplementary Fig. 15d). We also studied the effect of the thickness of Si pellets on the maximum strain under external biaxial tension. It is shown that thinner Si pellets experience higher strain (Supplementary Fig. 15e), which indicates that the yield might decrease if Si pellets are very thin. Supplementary Fig. 16 shows the effect of Young's modulus of the elastomeric balloon on the maximum strain of the Si pellet. The maximum strain increases monotonically with the Young's modulus of the elastomer. Therefore, softer balloon stamps or coating layers are expected to lower the strain level in Si pellets, which could improve the yield of the CAS printing process.

Hemispherical photodetector array by CAS printing

A convex-shaped photodetector array has implications in promising yet technically challenging and unusual imaging devices, for example, a wide-angle-of-view imager. We demonstrated an array of Si photodetectors on a hemispherical shell by CAS printing. The Si photodetector was structured into two p–n junctions in a back-to-back (n^+–p^-–p^-–n^+) configuration. The array (39 × 39, each Si photodetector size 100 μm × 100 μm) was fabricated by selective doping to define the p–n junctions and then the same was done for the Si pellets. The processes are schematically shown in Supplementary Fig. 17 and also described in the Methods. Figure 2a,b shows the optical images of the Si photodetector array on an Ecoflex hemispherical shell. The inset of Fig. 2a shows the photodetector array on the wafer before CAS printing. The performances of the photodetectors on the hemispherical shell were examined as shown in Supplementary Fig. 18. The current versus voltage (I–V) characteristics of the photodetector before (on the rigid substrate) and after (on the hemispherical shell) transfer printing are shown in Fig. 2c. The photocurrent under illumination was 0.15 μA and the dark current was 449 pA at a 3 V bias. The calculated current ratio $\Delta I/I_0$ is 3.33×10^2 at a 3 V bias, which is defined by the ratio between photocurrent (current under illumination ($I_{\text{illumination}}$) – current in the dark (I_{dark})) and I_{dark} (refs. [28,34,35]). The dynamic photocurrent responses of the device before and after CAS printing were measured at a constant bias of 3 V for 35 s while the light was respectively turned on and off. We measured and compared the device characteristics before and after CAS printing at different locations. They are fairly consistent and independent of location. As shown in Fig. 2d,e, no significant performance difference was observed after CAS printing on a curvy surface compared with those on the wafer, which further verifies that the strain on the Si photodetector is negligible.

Curvy helix antenna

Compact-sized (in the millimetre to centimetre range) electrically small antennas in 3D curvy shapes are an important class of devices for many applications[10,36,37]. However, efficiently manufacturing them in a simple yet precise manner has been a longstanding challenge[38]. We demonstrated a convex-shaped, four-armed helix antenna based on CAS printing. The 3D helix antenna fabrication involves pre-fabricating the antenna in a planar format and then CAS printing into a hemispherical convex shape. The fabrication began with laminating 5-μm-thick copper foil on a polydimethylsiloxane (PDMS) (Sylgard 184)-coated glass substrate, patterning by conventional photolithography, and a wet etching process. The detailed fabrication process is illustrated in Supplementary Fig. 19 and in the Methods. Using CAS printing, the antenna was successfully printed onto an Ecoflex hemispherical shell as shown in Fig. 2f. The inset of Fig. 2f shows an optical image of the pre-fabricated helix antenna on a glass substrate. Supplementary Fig. 20 shows the characterization setup, where one arm was soldered to the inner conductor of an SMA connector, and the other three arms were soldered to a circular copper ground plane with a radius of 9.2 cm. Figure 2g shows the measured reflection coefficient S_{11}. The resonant frequency is 4.09 GHz and the half power bandwidth is 13.94%. The half power bandwidth is lower than −3 dB. The results clearly show a simple way of accomplishing a 3D helix antenna based on CAS printing.

Hemispherical solar cell

Solar cells in spherical or hemispherical shapes have unique advantages in terms of wide-angle light harvesting compared with conventional planar devices[39–41]. We demonstrated a hemispherical, thin Si-based solar cell using CAS printing. The solar cell employs Si p–i–n junction devices connected in parallel and was pre-fabricated by selective doping, photolithography, RIE, anchor formation and undercut etching on an SOI wafer. Then, the device array was transferred onto a thin polyimide (PI) film (~1.5 μm thick) on a glass substrate by a PDMS stamp[27,42]. Thereafter, Au interconnects for the parallel connections were formed by e-beam evaporation and followed by PI encapsulation and patterning. The detailed device fabrication is described in the Methods and schematically shown in Supplementary Fig. 21. The patterned p–i–n Si solar cell array was released by buffer oxide etchant (BOE) (6:1) and transferred to a temporary glass substrate as shown in Supplementary Fig. 22. The solar cell is designed in the fashion of Si device pixels with serpentine-shaped interconnects, which are able to accommodate the large deformation during the CAS process without cracking the brittle Si devices. Finally, the solar cell array was printed onto a hemispherical PDMS shell through CAS printing as shown in Supplementary Fig. 23. Figure 3a provides a photograph of the hemispherical solar cell array and Fig. 3b shows an optical microscope image of the interconnected solar cell pixels on the hemispherical shell. FEA was performed to evaluate the strain on the device. Figure 3c presents the optical image of the Si p–i–n solar cell array and the corresponding FEA simulated strain distribution. The interconnection experienced a maximum principal strain of ~1.48% due to the deformation of the device array during the CAS printing process. However, the maximum principal strain for Si is ~0.18% (Fig. 3d). In addition, the intrinsic Si region experienced negligible strain.

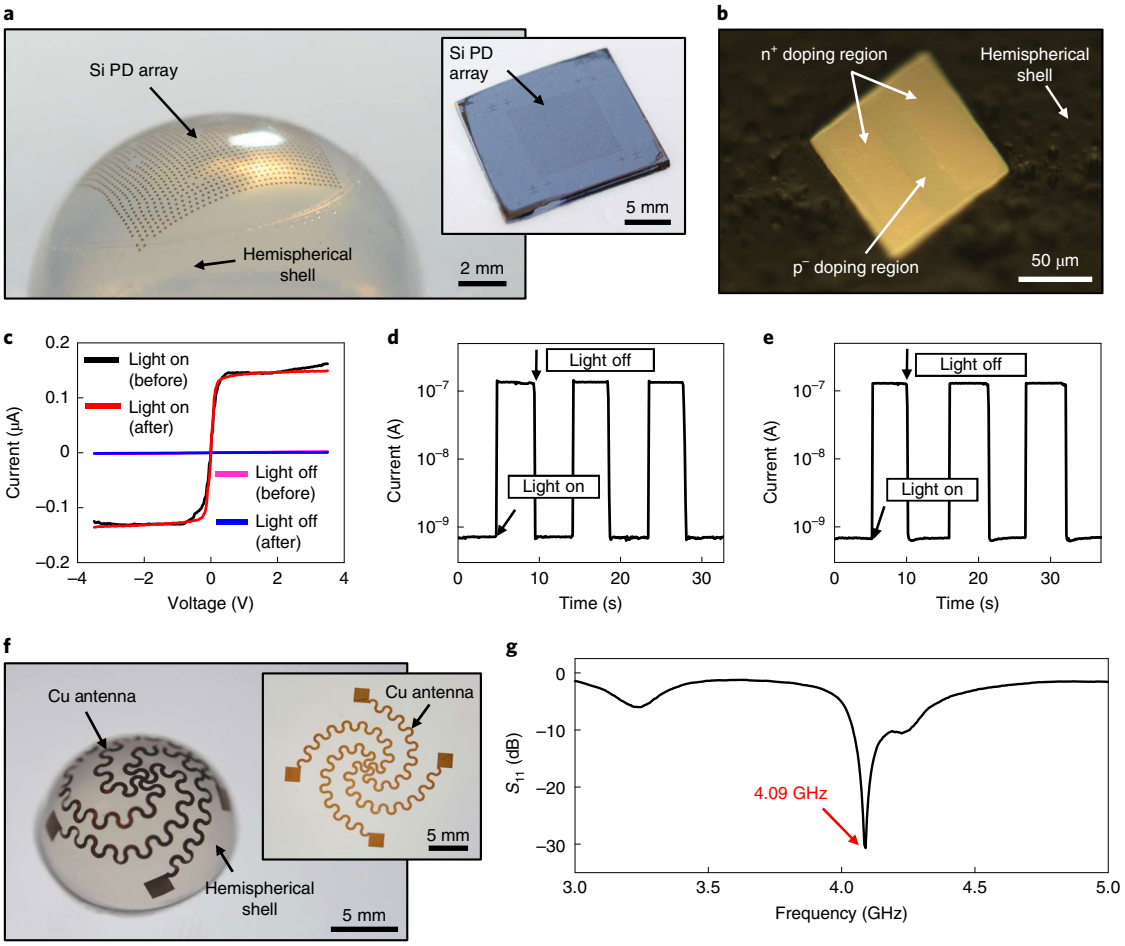

Fig. 2 | Devices on a hemispherical shell by CAS printing. a, A photograph of the Si photodetector (PD) array on a hemispherical shell after CAS printing. Inset: photodetector array on an SOI substrate. **b**, An optical microscope image of one single Si photodetector on a hemispherical shell. **c**, *I*–*V* curves of the photodetector under illumination and in the dark before and after CAS printing. **d**,**e**, Dynamic photoelectrical responses of the photodetector before (**d**) and after (**e**) CAS printing. **f**, An optical image of a 3D Cu helix antenna fabricated by CAS printing. Inset: optical image of a Cu helix antenna on a planar substrate. **g**, The measured reflection coefficient S_{11} of the 3D helix antenna. The red arrow indicates the resonant frequency.

The hemispherical solar cell was tested under 100 mW cm^{-2} (1 Sun) in ambient conditions. The current density versus voltage (*J*–*V*) characteristic of a single p–i–n pixel is shown in Fig. 3e. The short circuit current density (J_{sc}), open circuit voltage (V_{oc}), fill factor (FF) and photocurrent-conversion efficiency are 14.46 mA cm^{-2}, 0.352 V, 50.39% and 2.56%, respectively. The *I*–*V* and output power–voltage curves of the single solar cell are shown in Supplementary Fig. 24. Figure 3f shows the output power–voltage curve of the interconnected solar cell array in a planar configuration before printing onto the hemispherical shell. The short circuit current (I_{sc}), V_{oc}, FF and maximum power are 0.66 mA, 0.303 V, 34.11% and 68.3 μW, respectively. After CAS printing, the yielded hemispherical solar cell was characterized under different incident angles of light (Supplementary Fig. 25). The *I*–*V* characteristics and output power–voltage curve of the hemispherical solar cell for different incident angles of light are shown in Supplementary Fig. 26 and Fig. 3f, respectively. The maximum output powers are 39.0 μW, 28.2 μW, 20.8 μW and 10.7 μW at 90°, 60°, 30° and 0° incident angles of light, respectively. The angle dependency of V_{oc} and output power is attributed to the change in illumination angle and thus the light intensity, and also the number of pixels under illumination[43]. It is noted that the maximum power of the hemispherical solar cell at an incident light angle of 90° is lower than that of a device in planar configuration due to the device footprint and thus the exposed area difference. Although the present design of a solar cell array with serpentine interconnection has a relatively low filling ratio, other structure designs could have a higher filling ratio.

Multifunctional contact lens

Contact lenses with enabled non-invasive health monitoring or imaging functions are promising smart wearable devices[44]. A prototype of a smart contact lens (Fig. 4a) with three different devices—(1) lactate sensor, (2) temperature sensor and (3) imager—was achieved using CAS printing onto the moulded PDMS lens model. Specifically, an unusually high L-lactate concentration in tears provides a possible indication of ischaemia, sepsis, liver disease and/or even cancer[6,45]. A significantly higher L-lactate concentration in tear fluid (1–5 mM) than that in blood (0.36–0.75 mM)[6] correspondingly makes the sensor development less challenging; therefore, it is advantageous to implement lactate sensing based on non-invasive contact lenses. The ocular surface temperature is one of the crucial parameters for diagnosing eye health conditions since it relates to blood-flow velocity in the ophthalmic artery[46]. Image capturing from a worn contact lens is a unique feature as it can either supplement or enable visual capabilities for the wearer. All sensors and the imager were pre-fabricated based on microfabrication, then printed onto a contact lens using CAS printing, as aforementioned for the other devices. The detailed fabrication process is described in the

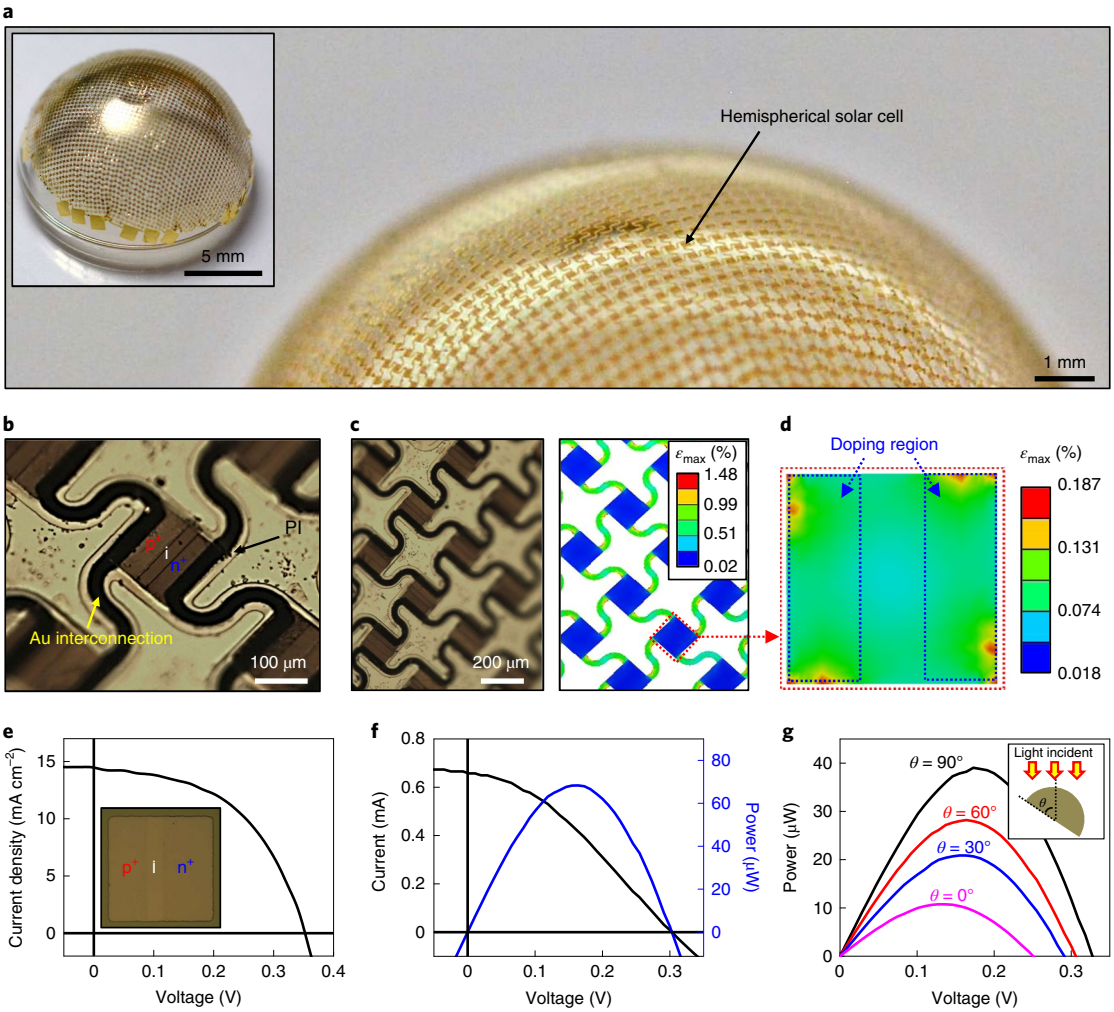

Fig. 3 | Hemispherical solar cell. a, An optical image of the Si-based p–i–n solar cell array on a hemispherical PDMS substrate after CAS printing. Inset: overall view of the p–i–n solar cell array on a hemispherical PDMS substrate. **b**, An optical microscope image of a single Si-based p–i–n solar cell. **c**, An optical microscope image of a Si-based p–i–n solar cell array on hemispherical substrate (left) and the corresponding FEA result (right). **d**, The FEA result of the maximum principal strain in the interconnected Si-based p–i–n solar cells. **e**, The *J*–*V* curve of a single p–i–n Si solar cell. Inset: optical microscope image of single solar cell before interconnection. **f**, The *I*–*V* curve and output power–voltage curve of the interconnected solar cell array on a planar substrate. **g**, Output power–voltage curve of the interconnected solar cell array on a hemispherical substrate after CAS printing for different incident angles of light. Inset: schematic of incident angle of light definition.

Methods and schematically shown in Supplementary Figs. 27–29. The successfully fabricated smart contact lens is shown in Fig. 4b.

The lactate sensor based on the amperometric mechanism was structured with three electrodes, including a working electrode (WE), a counter electrode (CE) and a reference electrode (RE). The WE and CE were designed into serpentine shapes to enable mechanical stretchability. A thin layer of lactate oxidase (LOx) as the enzyme on the electrodes is shown in Fig. 4c. It is noted that good stability of immobilized LOx through cross-liking of the amine group of the enzyme with an insoluble carrier, bovine serum albumin (BSA), by glutaradehyde (GTA) has been reported elsewhere[45,47,48]. The inset of Fig. 4c schematically shows the sensing mechanism. The details are described in Supplementary Note 3. The amperometric measurements were performed with a constant potential of 400 mV at the RE by varying the concentration of the L-lactate solution. Continuous sensing of tear L-lactate concentration in the physiological range (1–5 mM)[6,45] was successfully achieved (Fig. 4d). It is noted that at relatively low concentrations (0.05–1.00 mM), a linear response between the current and concentration was observed (Supplementary Fig. 30). At higher concentrations (1–50 mM), a nonlinear relationship was observed (Supplementary Fig. 31). The calculated sensitivity and limit of detection (LOD) of the sensor are 9.39 μA mM^{-1} cm^{-2} and 4.57 μM, respectively. The measurements were further compared with the Michaelis–Menten kinetic model[45,49]. Specifically, the Michaelis–Menten constant (K_M) and I_{max} were extracted from Supplementary Fig. 31a using the Lineweaver–Burk equation and the values are 1.23 mM and 113.62 nA, respectively[49,50]. The detailed calculations are described in Supplementary Note 4. The fitting curve of the Michaelis–Menten kinetic model is in good agreement with the measurements, as shown in Fig. 4e and Supplementary Fig. 31b. The results suggest that the contact lens with a lactate sensor is feasible for continuous monitoring of the L-lactate level in tear fluid. Although the lactate sensor can retain sensitivity over a relatively short period of time[45], such as minutes to hours, degradation in the long term (from days to months) was observed[51]. It is worth mentioning that neither delamination between the multifunctional device and the lens model nor delamination between the enzyme and sensing electrodes was observed.

The temperature sensor for ocular surface temperature monitoring was based on a Si p–i–n diode. The device is interconnected with

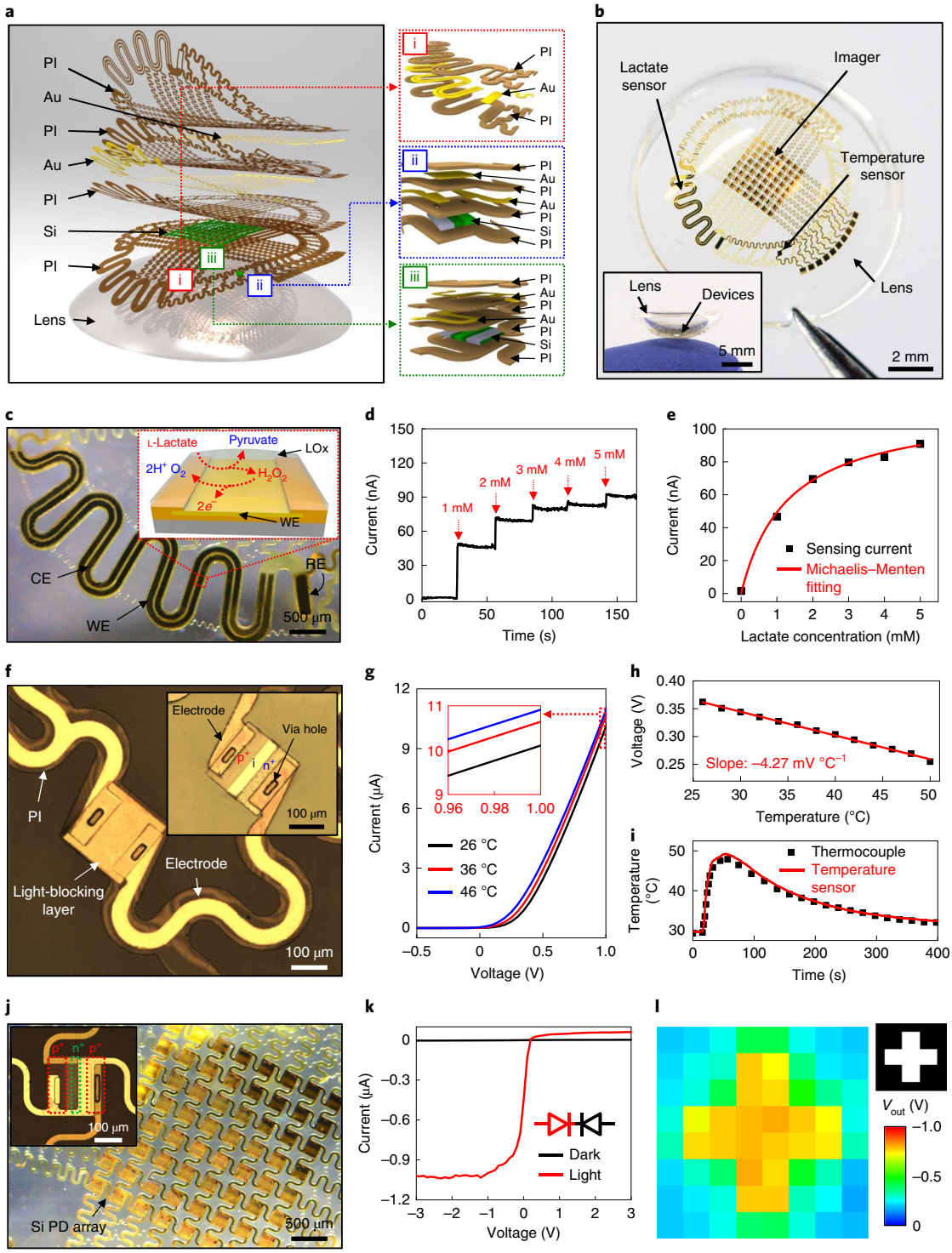

Fig. 4 | Multiple functional smart contact lens electronics. a, Schematic of the contact lens electronics. **b**, Optical image of the contact lens electronics. Inset: side view of the electronics. **c**, Optical microscope image of the lactate sensor. Inset: schematic of the sensing mechanism. **d**, Continuous sensing properties at different L-lactate concentrations. **e**, Calibration curve of the lactate sensor in the physiological range (1–5 mM) with a fitting curve from the Michaelis–Menten model. **f**, Optical microscope image of the Si temperature sensor. Inset: device before formation of the light-blocking layer. **g**, *I*–*V* characteristics of the temperature sensor at different representative temperatures. **h**, Calibration curve of Si temperature sensor. **i**, Plots of temperature sensing by using a commercially available thermocouple and Si-based temperature sensor. **j**, Optical microscope image of the imaging sensor array on the contact lens. Inset: optical microscope image of a single pixel. **k**, Representative *I*–*V* curve of a single pixel under illumination (light, red) and in the dark (black). **l**, Output voltage (V_{out}) mapping result of the imaging sensor array under the patterned illumination through a photomask. Inset: shape of photomask.

serpentine electrodes, as shown in Fig. 4f. A light-blocking layer of metal was used to eliminate any photoresponse. Figure 4g shows the *I*–*V* curves of the diode temperature sensor under different temperatures (26 °C, 36 °C and 46 °C). Clear temperature dependency on the forward bias current was shown[52,53]. The calibration curve was obtained by extracting voltage at 1 μA from the *I*–*V*

curves under different temperatures as shown in Supplementary Fig. 32. Figure 4i shows continuous temperature sensing based on the diode sensor. The result matches well with that of a thermocouple (Fluke 80PK-1 Bead Probe).

The imager was designed with 8×8 arrayed photodetecting pixels (Fig. 4j). The individual pixel consists of a Si p–i–n photodiode and n–i–p multiplexing diode configured in a back-to-back fashion. The multiplexing diode has a metal light-blocking layer to eliminate its light response (inset of Fig. 4j). Figure 4k shows the *I*–*V* curves of an individual pixel under illumination and in the dark with a photocurrent of 1.02 μA and a dark current of 3.95 nA. Supplementary Fig. 33 shows the circuit diagram of the imager with the detector array, where shunt resistors (5 MΩ) were used for voltage measurement purposes. It is noted that −1 V was applied to each column during readout. The dynamic output voltage upon repeatedly turning the light on and off for a single pixel is shown in Supplementary Fig. 34. Multiplexing-enabled voltage mapping from patterned light illumination through a photomask was obtained using a data acquisition system (DAQ, National Instruments)[54]. Figure 4l illustrates the voltage mapping based on illumination through a 'cross'-shaped photomask (inset). While the current imager is opaque and thus may block the view, careful device designs can be further implemented to obtain a transparent format or a lens that does not cover the visual zone to yield a see-through contact lens.

CAS printing on arbitrary curvy surfaces

Although several different hemispherical or similarly shaped devices were demonstrated, we further validated the versatility and fidelity of CAS printing devices onto arbitrary 3D surfaces. Serpentine-shaped meshes (Supplementary Fig. 35; overall size 11.2 mm×11.2 mm) with a metal layer sandwiched between two PI layers were used. The processes of mesh fabrication are described in the Methods and schematically shown in Supplementary Fig. 36. Various 3D curvy surfaces including concave, wavy, convex edge, concave edge, pyramid and uneven surface were prepared with a thin adhesive layer of Ecoflex. The meshes were successfully printed onto these curvy substrates as shown in Fig. 5a–f. The versatility of CAS printing onto arbitrary curvy or uneven substrates is due to the conformal contact between the stamp and target surfaces. FEA was also carried out to simulate the deformation and strain within the stamp and mesh. The relative displacement contour of the mesh on the stamp after picking up is shown in Supplementary Fig. 37. In addition, the strain distributions of the balloon, coating layer and mesh on the balloon stamp are shown in Supplementary Fig. 38. The strain distribution of the balloon and coating layer during CAS printing onto concave and screwdriver handle wavy surfaces is illustrated in Supplementary Fig. 39 (concave) and Supplementary Fig. 40 (wavy).

The bottom panels of Fig. 5a,b show the strain distribution in the metal layer after printing onto the concave and screwdriver handle wavy surfaces, respectively. The maximum strain in Fig. 5a is ~1.33% near the corners, which is because the serpentine mesh is mainly subject to bending with relatively large stretching in the four corners (Supplementary Fig. 41). Compared with the concave substrate, the screwdriver handle has sharper edges, causing more severe deformation in the metal mesh during the CAS printing process as shown in Fig. 5b and Supplementary Figs. 40 and 42. The maximum strain in the metal mesh is 3.28%, appearing on the edges. The mesh near the edges of the handle is subjected to a combination of bending and stretching. These results evidentially suggest that CAS printing induces tolerant strain into devices and can be employed as a generalized platform for devices with various curvy shapes.

Conclusions

We have reported CAS printing for manufacturing 3D curvy electronics. The technology has been used to manufacture devices with both isolated pixels (such as thin Si pellets and photodetector arrays) and interconnected functional devices (such as antennas, hemispherical solar cells and smart contact lenses). By taking advantage of traditional electronics fabrication, the approach can create 3D curvy electronic devices that outperform devices built with existing 3D printing technologies, which use liquid- or semi-liquid-based electronic materials[8]. The excellent deformability of the balloon stamp is a key feature of CAS printing and means that it is can print onto arbitrary 3D surfaces. As a result, our technology could be used to create novel devices and systems for application in a variety of fields, including optoelectronics, telecommunication and medicine.

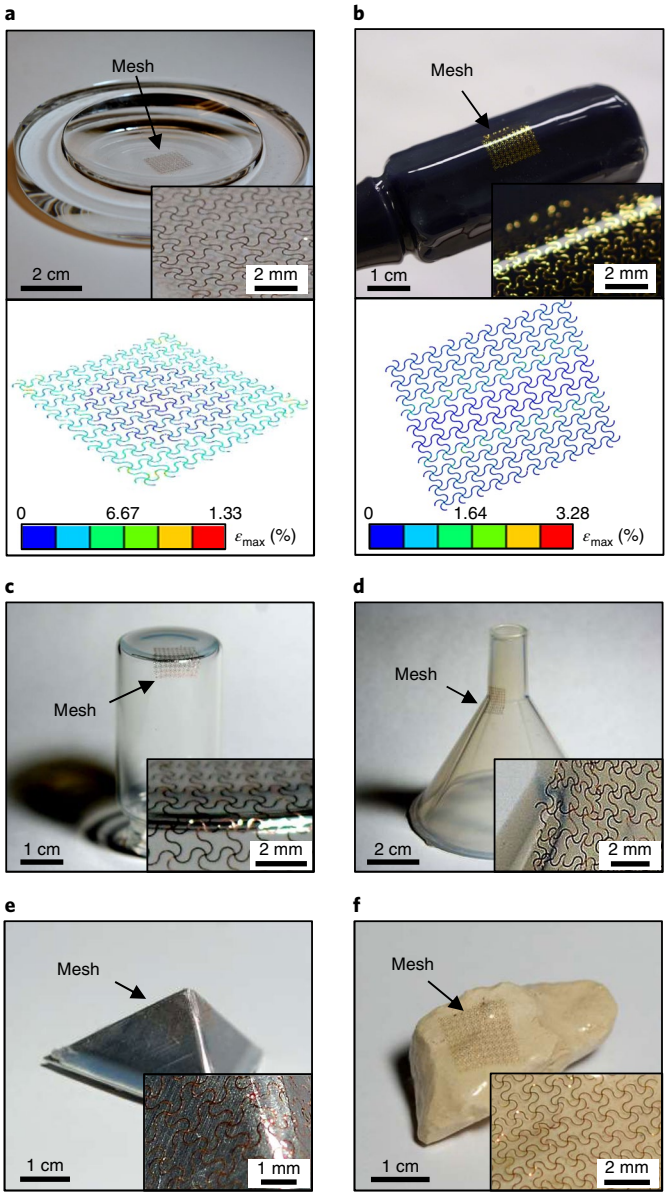

Fig. 5 | CAS printing onto various 3D curvilinear substrates. a–f, Optical images of the serpentine metal mesh on concave (**a**, top), wavy (**b**, top), convex edge (**c**), concave edge (**d**), pyramid (**e**) and uneven surfaces (**f**) by CAS printing. FEA results of the serpentine metal mesh on concave (**a**, bottom) and wavy (**b**, bottom) surfaces by CAS printing. Insets: optical images with magnified view.

Methods

Conformal balloon stamp preparation. The balloon stamp was prepared by inflating a latex balloon. Liquid Clearflex precursor (Smooth-ON, Clear Flex 50)

was coated on the inflated balloon and pre-cured at room temperature for 16 h and then fully cured at 60 °C for 5 h.

Hemispherical shell preparation. The hemispherical shell was prepared using a custom-made mould. Liquid silicone, such as Ecoflex (Smooth-On Ecoflex 00-30) or PDMS (Sylgard 184, ratio of monomer to cross-linker is 10:1), was poured into a concave mould. Then a convex mould was pressed against the concave mould with a 1-mm-thick spacer. The mould was heated at 90 °C to solidify for 20 min or 60 min for Ecoflex or PDMS, respectively. Finally, the shell was retrieved by separating the moulds.

Si pellet array fabrication. The Si pellet array was prepared from an SOI wafer with 1.25-μm-thick single crystalline Si on top. The fabrication of the 39 × 39 array of Si square pellets (100 μm × 100 μm) was started by photolithography to define the geometries. The photolithography process involved spin-coating of photoresist (AZ 5214) on the SOI wafer at 2,000 r.p.m. for 30 s and baking on a hotplate at 110 °C for 90 s, followed by ultraviolet exposure ($\lambda = 365$ μm) with a dose of 200 mJ cm^{-2}, and developing through MIF917 for 1 min. Thereafter, the Si pellet array was patterned by RIE by sulfur hexafluoride with a gas flow of 100 s.c.c.m. for 1 min. The photoresist anchors for Si pellets were formed by photolithography after etching the exposed SiO_2 by BOE (6:1) to prevent the floating away of the pellet after fully undercut etching of the SiO_2. The Si pellet array was immersed in concentrated hydrofluoric acid (49%) for 90 min to fully remove the buried SiO_2.

Si photodetector fabrication. The Si-based photodetector array fabrication began with cleaning the SOI wafer with 1.25-μm-thick top Si layer (p-type, resistivity: 11.5 Ω cm) for selective doping. A 300-nm-thick SiO_2-based doping mask was formed on the SOI wafer using spin-on-glass (700B, Filmtronics), followed by annealing at 700 °C for 4 min in N_2 atmosphere. The doping windows were opened by photolithography and wet etching in BOE (6:1) for 1 min. The phosphorous-based spin-on-dopant (P510, Filmtronics) was coated and annealed at 950 °C to form two back-to-back n^+–p^-–p^-–n^+ diodes. The photodetector array was patterned and released from the Si wafer following the same procedures for the Si pellet array.

Copper antenna fabrication. The antenna was accomplished by fabricating on a temporary substrate of PDMS. PDMS precursor solution (Sylgard 184, ratio of monomer to cross-linker is 10:1) was spin-coated on a glass substrate followed by half-curing at 100 °C for 30 s. A 5-μm-thick copper foil was carefully laminated on top of the PDMS/grass substrate followed by full curing to ensure stable bonding. The antenna was patterned through photolithography and wet etching by copper etchant. The antenna was picked up using scotch tape and released onto a glass substrate in acetone solution[26].

Silicon solar cell array. The fabrication of the Si solar cell follows similar steps to those for the photodetectors, except both n- and p-type doping are performed. Spin-on-glass (700B, Filmtronics) was used as the doping mask and p-type doping was first processed using boron-based spin-on-dopant (B155, Filmtronics) annealed at 950 °C. The dopant residue and SiO_2 doping mask was removed by concentrated hydrofluoric acid. The n-doping mask was formed by spin-on-glass and the n-doping was based on spin-on-dopant (P510, Filmtronics). The spacing between p-doping and n-doping was 30 μm; thus, the intrinsic region for light harvesting is defined as 4.5×10^{-5} cm^2. The top Si device was patterned into 150 μm × 150 μm square arrays by RIE using sulfur hexafluoride gas (100 s.c.c.m. for 1 min). The released p–i–n solar cell array was picked up by a PDMS stamp (~8 mm thickness) and transfer printed on top of a half-cured PI layer on a glass substrate. The PI was then fully cured at 250 °C for 1 h. Interconnects of chromium (5 nm) and gold (200 nm) were deposited on the transferred devices array using an e-beam evaporator and patterned by photolithography. Then, devices were encapsulated by another PI using spin-casting, photolithography and RIE etching in O_2 plasma. Finally, the solar cell array was released from the glass substrate by immersion in BOE solution.

Multifunctional contact lens fabrication. The contact lens electronics with multiple functions (lactate sensing, temperature sensing and imaging sensing) was fabricated through a similar process to the abovementioned photodetector array and p–i–n solar cells. The three sensors were fabricated simultaneously. The fabrication process began with selective doping of Si on an SOI wafer and transfer printing onto a half-cured PI substrate as mentioned above. After transfer printing, the PI was fully cured at 250 °C for 1 h. Then a PI interlayer was coated and the via holes were formed using RIE (O_2, 40 s.c.c.m., 150 mtorr, 250 W, 10 min). The first interconnecting metal (chromium/gold, 5/200 nm) was formed using e-beam evaporation, photolithography and wet etching. Then, a second PI layer and the via holes were formed, followed by a second metallization (chromium/gold, 5/200 nm) for another interconnection and light-blocking layer to block the diode and temperature sensor. Thereafter, an encapsulating PI layer was coated on top of the devices and cured. The devices were patterned using O_2 plasma through a SiO_2 mask that was formed by e-beam evaporation and photolithography. The thin device was then separated from the glass substrate using BOE (6:1). The separated device was first retrieved by a poly(methylmethacrylate)-coated substrate followed by SiO_2 deposition. A balloon stamp then finally picked up the device upon poly(methylmethacrylate) removal in acetone and the device was printed onto an ultraviolet ozone-treated contact lens model, followed by thermal treatment at 90 °C to form irreversible bonding. To form LOx on the lactate sensor electrodes, the LOx was immobilized by covalent cross-linking of the enzyme and BSA by GTA[45,47,48]. Next, 2.55 mg BSA (≥98%, lyophilized powder, Sigma Aldrich) was dissolved in 79.73 μl phosphate buffer solution. Then, 1.02 μl GTA (25% in H_2O, Grade I, Sigma Aldrich) and 1.7 mg lactate oxidase from *Aerococcus viridans* (50UN, lyophilized powder, Sigma Aldrich) were added to the solution. The solution was dropped onto the electrodes and then dried for 1 h at room temperature.

Serpentine mesh fabrication. The mesh started by coating with PI precursor solution and curing at 250 °C for 1 h. A 200 nm copper layer was deposited on the PI by an e-beam evaporator. The gold layer was then patterned by photolithography and wet etching. The PI with metal on top was finally patterned and released from the glass substrate.

Si photodetector characterization. Electrical characteristics of Si photodetectors were measured by a Keithley 2400 source meter with an Imagelite model 20 illuminator (Stocher & Yale) light source at room temperature under ambient conditions. The photocurrent of Si photodetector was characterized under vertically shined visible light with intensity of 1 klx.

Copper antenna characterization. The reflection coefficient of the helix antenna was measured by a National Instrument PXIe-5630 vector network analyser in free space. The antenna was placed on a copper ground and fed by an SMA probe.

Hemispherical solar cell characterization. The *J*–*V* curves and output power of the p–i–n Si solar cells were characterized under 1 Sun light conditions using a Keithley 2400 source meter and a solar simulator (ORIEL Instruments, Sol3A). A standard silicon solar cell (ORIEL, 91150V) was used to calibrate the power of the 1 Sun simulated light (100 mW cm^{-2}). Hemispherical solar cell performance at different light incident angles was measured by tilting the device.

Data availability

The data that support the plots within this paper and other findings of this study are available from the corresponding author upon reasonable request.

Received: 3 April 2019; Accepted: 19 August 2019;
Published online: 23 September 2019

References

1. Dinyari, R., Rim, S.-B., Huang, K., Catrysse, P. B. & Peumans, P. Curving monolithic silicon for nonplanar focal plane array applications. *Appl. Phys. Lett.* **92**, 091114 (2008).
2. Hung, P. J., Jeong, K., Liu, G. L. & Lee, L. P. Microfabricated suspensions for electrical connections on the tunable elastomer membrane. *Appl. Phys. Lett.* **85**, 6051–6053 (2004).
3. Song, Y. M. et al. Digital cameras with designs inspired by the arthropod eye. *Nature* **497**, 95–99 (2013).
4. Jeong, K.-H., Kim, J. & Lee, L. P. Biologically inspired artificial compound eyes. *Science* **312**, 557–561 (2006).
5. Kim, J. et al. Wearable smart sensor systems integrated on soft contact lenses for wireless ocular diagnostics. *Nat. Commun.* **8**, 14997 (2017).
6. Farandos, N. M., Yetisen, A. K., Monteiro, M. J., Lowe, C. R. & Yun, S. H. Contact lens sensors in ocular diagnostics. *Adv. Healthc. Mater.* **4**, 792–810 (2015).
7. Vásquez Quintero, A., Verplancke, R., De Smet, H. & Vanfleteren, J. Stretchable electronic platform for soft and smart contact lens applications. *Adv. Mater. Technol.* **2**, 1700073 (2017).
8. Adams, J. J. et al. Conformal printing of electrically small antennas on three-dimensional surfaces. *Adv. Mater.* **23**, 1335–1340 (2011).
9. Kim, O. S. Low-Q electrically small spherical magnetic dipole antennas. *IEEE Trans. Antennas Propag.* **58**, 2210–2217 (2010).
10. Abadia, J., Merli, F., Zurcher, J.-F., Mosig, J. R. & Skrivervik, A. K. 3D-spiral small antenna design and realization for biomedical telemetry in the MICS band. *Radioengineering* **18**, 359–367 (2009).
11. Boncheva, M. et al. Magnetic self-assembly of three-dimensional surfaces from planar sheets. *Proc. Natl Acad. Sci. USA* **102**, 3924–3929 (2005).
12. Guo, X. et al. Two-and three-dimensional folding of thin film single-crystalline silicon for photovoltaic power applications. *Proc. Natl Acad. Sci. USA* **106**, 20149–20154 (2009).
13. Xu, W. et al. Ultrathin thermoresponsive self-folding 3D graphene. *Sci. Adv.* **3**, e1701084 (2017).
14. Liu, Y., Shaw, B., Dickey, M. D. & Genzer, J. Sequential self-folding of polymer sheets. *Sci. Adv.* **3**, e1602417 (2017).
15. Mei, J., Lovell, M. R. & Mickle, M. H. Formulation and processing of novel conductive solution inks in continuous inkjet printing of 3-D electric circuits. *IEEE Trans. Electron. Packag. Manuf.* **28**, 265–273 (2005).

16. Seong, B. et al. Metal-mesh based transparent electrode on a 3-D curved surface by electrohydrodynamic jet printing. *J. Micromech. Microeng.* **24**, 097002 (2014).
17. An, B. W. et al. Direct printing of reduced graphene oxide on planar or highly curved surfaces with high resolutions using electrohydrodynamics. *Small* **11**, 2263–2268 (2015).
18. Lee, S. et al. Electroless deposition-assisted 3D printing of micro circuitries for structural electronics. *ACS Appl. Mater. Interfaces* **11**, 7123–7130 (2019).
19. Tan, H. W., An, J., Chua, C. K. & Tran, T. Metallic nanoparticle inks for 3D printing of electronics. *Adv. Electron. Mater.* **5**, 1800831 (2019).
20. Mohammed, M. G. & Kramer, R. All-printed flexible and stretchable electronics. *Adv. Mater.* **29**, 1604965 (2017).
21. Kwon, J. et al. Three-dimensional monolithic integration in flexible printed organic transistors. *Nat. Commun.* **10**, 54 (2019).
22. Ko, H. C. et al. Curvilinear electronics formed using silicon membrane circuits and elastomeric transfer elements. *Small* **5**, 2703–2709 (2009).
23. Ko, H. C. et al. A hemispherical electronic eye camera based on compressible silicon optoelectronics. *Nature* **454**, 748–753 (2008).
24. Huang, C. C. et al. Large field of view wide spectrum artificial reflecting superposition compound eyes. *Small* **10**, 3050–3057 (2014).
25. Wu, H. et al. Conformal pad-printing electrically conductive composites onto thermoplastic hemispheres: toward sustainable fabrication of 3-cents volumetric electrically small antennas. *PLoS ONE* **10**, e0136939 (2015).
26. Sim, K. et al. High fidelity tape transfer printing based on chemically induced adhesive strength modulation. *Sci. Rep.* **5**, 16133 (2015).
27. Sim, K., Li, Y., Song, J. & Yu, C. Biaxially stretchable ultrathin Si enabled by serpentine structures on prestrained elastomers. *Adv. Mater. Technol.* **4**, 1800489 (2019).
28. Sim, K., Rao, Z., Li, Y., Yang, D. & Yu, C. Curvy surface conformal ultra-thin transfer printed Si optoelectronic penetrating microprobe arrays. *npj Flex. Electron.* **2**, 2 (2018).
29. Gao, Y. et al. Crack-insensitive wearable electronics enabled through high-strength kevlar fabrics. *IEEE Trans. Compon. Packag. Manuf. Technol.* **5**, 1230–1236 (2015).
30. Xu, S. et al. Assembly of micro/nanomaterials into complex, three-dimensional architectures by compressive buckling. *Science* **347**, 154–159 (2015).
31. Wang, X. et al. Freestanding 3D mesostructures, functional devices, and shape-programmable systems based on mechanically induced assembly with shape memory polymers. *Adv. Mater.* **31**, 1805615 (2019).
32. Zhang, Y. et al. A mechanically driven form of kirigami as a route to 3D mesostructures in micro/nanomembranes. *Proc. Natl Acad. Sci. USA* **112**, 11757–11764 (2015).
33. Humood, M. et al. Fabrication and deformation of 3D multilayered kirigami microstructures. *Small* **14**, 1703852 (2018).
34. Qian, C. et al. High-performance organic heterojunction phototransistors based on highly ordered copper phthalocyanine/para-sexiphenyl thin films. *Adv. Funct. Mater.* **27**, 1604933 (2017).
35. Noh, Y.-Y., Kim, D.-Y. & Yase, K. Highly sensitive thin-film organic phototransistors: effect of wavelength of light source on device performance. *J. Appl. Phys.* **98**, 074505 (2005).
36. Adams, J., Slimmer, S. C., Lewis, J. & Bernhard, J. 3D-printed spherical dipole antenna integrated on small RF node. *Electron. Lett.* **51**, 661–662 (2015).
37. Toriz-Garcia, J. et al. Fabrication of a 3D electrically small antenna using holographic photolithography. *J. Micromech. Microeng.* **23**, 055010 (2013).
38. Liu, F. et al. High performance, tunable electrically small antennas through mechanically guided 3D assembly. *Small* **15**, 1804055 (2019).
39. Lamoureux, A., Lee, K., Shlian, M., Forrest, S. R. & Shtein, M. Dynamic kirigami structures for integrated solar tracking. *Nat. Commun.* **6**, 8092 (2015).
40. Maruyama, T. & Minami, H. Light trapping in spherical silicon solar cell module. *Sol. Energy Mater. Sol. Cells* **79**, 113–124 (2003).
41. Minemoto, T., Murozono, M., Yamaguchi, Y., Takakura, H. & Hamakawa, Y. Design strategy and development of spherical silicon solar cell with semi-concentration reflector system. *Sol. Energy Mater. Sol. Cells* **90**, 3009–3013 (2006).
42. Meitl, M. A. et al. Transfer printing by kinetic control of adhesion to an elastomeric stamp. *Nat. Mater.* **5**, 33–38 (2005).
43. Markvart, T. & Castaner, L. in *Solar Cells: Materials, Manufacture and Operation* 2nd edn (eds McEvoy, A. et al.) Ch. IA-1 (Academic Press, 2012).
44. Park, J. et al. Soft, smart contact lenses with integrations of wireless circuits, glucose sensors, and displays. *Sci. Adv.* **4**, eaap9841 (2018).
45. Thomas, N., Lähdesmäki, I. & Parviz, B. A. A contact lens with an integrated lactate sensor. *Sens. Actuators B* **162**, 128–134 (2012).
46. Gugleta, K., Orgül, S. & Flammer, J. Is corneal temperature correlated with blood-flow velocity in the ophthalmic artery? *Curr. Eye Res.* **19**, 496–501 (1999).
47. House, J. L., Anderson, E. M. & Ward, W. K. Immobilization techniques to avoid enzyme loss from oxidase-based biosensors: a one-year study. *J. Diabetes Sci. Technol.* **1**, 18–27 (2007).
48. Marzouk, S. A. et al. Amperometric monitoring of lactate accumulation in rabbit ischemic myocardium. *Talanta* **44**, 1527–1541 (1997).
49. Kausaite-Minkstimiene, A., Mazeiko, V., Ramanaviciene, A. & Ramanavicius, A. Enzymatically synthesized polyaniline layer for extension of linear detection region of amperometric glucose biosensor. *Biosens. Bioelectron.* **26**, 790–797 (2010).
50. Yu, J., Liu, S. & Ju, H. Glucose sensor for flow injection analysis of serum glucose based on immobilization of glucose oxidase in titania sol–gel membrane. *Biosens. Bioelectron.* **19**, 401–409 (2003).
51. Puggioni, G. et al. Low-temperature storage improves the over-time stability of implantable glucose and lactate biosensors. *Sensors* **19**, 422 (2019).
52. Kim, J. et al. Stretchable silicon nanoribbon electronics for skin prosthesis. *Nat. Commun.* **5**, 5747 (2014).
53. Webb, R. C. et al. Ultrathin conformal devices for precise and continuous thermal characterization of human skin. *Nat. Mater.* **12**, 938–944 (2013).
54. Yu, C. et al. Adaptive optoelectronic camouflage systems with designs inspired by cephalopod skins. *Proc. Natl Acad. Sci. USA* **111**, 12998–13003 (2014).

Acknowledgements

C.Y. thanks the funding support by National Science Foundation (ECCS-1509763 and CMMI-1554499), startup fund and the Bill D. Cook faculty scholarship from the Department of Mechanical Engineering at University of Houston.

Author contributions

K.S., S.C. and C.Y. conceived and designed the experiment. K.S., S.C., Z.R., J.L., Y.L. and S.J. performed the experiment. Z.L. and J.X. performed numerical analysis. K.S., J.C. and C.Y. analysed experimental data. K.S., Z.L., J.X., F.E. and C.Y. wrote the paper.

Competing interests

The authors declare no competing interests.

Additional information

Supplementary information is available for this paper at https://doi.org/10.1038/s41928-019-0304-4.

Correspondence and requests for materials should be addressed to C.Y.

Reprints and permissions information is available at www.nature.com/reprints.

Publisher's note Springer Nature remains neutral with regard to jurisdictional claims in published maps and institutional affiliations.